EDITED BY CAROLINE ASH

Ammonite, Reconstructed > >

Ammonites were an abundant marine organism that went extinct about the same time as the dinosaurs—roughly 65 million years ago. Although their shells make good fossils, other ammonite structures are rarely discerned. **Kruta *et al.*** (p. 70; see the Perspective by **Tanabe**) have used synchrotron-based x-ray microtomography to visualize and reconstruct the mouthparts of three specimens. The morphology of the jaws and radula suggests that ammonites fed on small marine invertebrates—indeed, tiny crustaceans and snail-like gastropods were found among the jaws of one specimen.

Heating the Solar Atmosphere

The question of why the Sun's outer atmosphere, or corona, is much hotter than its surface is one of the main unresolved issues in solar astrophysics. By combining measurements from NASA's Solar Dynamics Observatory and the Japanese Hinode satellite, **De Pontieu *et al.*** (p. 55) show that jets of plasma propelled upward from the region immediately above the Sun's surface are implicated in the heating of the solar corona. The results challenge current models for coronal heating and show that the interface region between the surface of the Sun and its corona plays a crucial role in energizing the solar atmosphere.

Spinning the Unspinnable

Weaving and spinning can take a weak material like straw or yarn and turn it into a much tougher rope. **Lima *et al.*** (p. 51) found that by using carbon nanotubes as a support material, they could spin and weave a range of materials that otherwise are considered intractable to such manipulation, ranging from superconductors to sutures containing biomedical agents. The desired materials were deposited onto a web of multiwalled carbon nanotubes, using an electrostatic powder coating gun, and then twisted into yarns, which could be knotted and sewn, and showed excellent retention of the guest particles when subjected to solvents or a mechanical washing cycle.

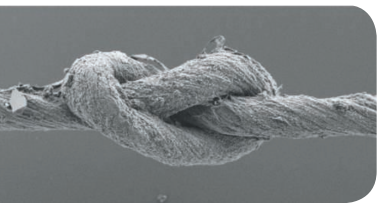

Toward Perfection?

When physicists tried to re-create the conditions believed to have existed microseconds after the Big Bang, they found, to their surprise, that the resulting "soup" of quarks and gluons behaved not like a gas, but like a perfect (frictionless) liquid. **Cao *et al.*** (p. 58, published online 9 December) have studied one such candidate for a perfect liquid at a convenient scale—a dilute gas of fermionic Li-6 atoms—and measured its viscosity in a wide temperature range. The results were consistent with expectations that a resonant Fermi gas would have properties dependent only on density and temperature. Although the estimated viscosity/entropy ratio approached the perfect fluid limit, it still exceeded it by fivefold. Nevertheless, these measurements can now be compared with advanced theoretical models.

Spinning for Naught

Large-scale structures or discontinuities in Earth's interior are typically caused by transformations in the physical or chemical properties of minerals that occur when pressure increases with depth. For example, an electronic spin transition in iron atoms within minerals that are stable at high pressures and temperatures has been predicted to influence some minerals' compressibility and, hence, the speed of sound waves passing through the lower mantle. Using an inelastic x-ray scattering technique at high pressures, **Antonangeli *et al.*** (p. 64) show that the spin transition in fact does not influence how ferropericlase (a major lower-mantle mineral) is compressed, but it does appear to affect anisotropy (i.e., directionally dependent properties) within ferropericlase, which may account for the observed directional dependence of some seismic waves in the lower mantle, even though the spin transition itself, which should occur at a defined depth, does not correspond to any specific structure or anomaly in the lower mantle.

Seasonal Behavioral Plasticity

The African butterfly *Bicyclus anynana* shows a sex-role reversal in courtship behavior, which is set during larval development and controlled by larval rearing temperature. In the wet season form, the males court and the females choose, while in the dry season form, females court and males choose. **Prudic *et al.*** (p. 73) show that these changes in mating behavior correlate with a cryptic change of the sexual ornament in both sexes. In the wet season, males have brighter sexual signal in the ultraviolet (UV) range, and in the dry season, females have a brighter sexual signal in the UV range. These changes in both sexual roles and signal are also correlated with a change in costs and benefits to mating among the different seasonal forms. Females have both increased longevity and reproductive output if they mate with dry season males, but dry season males have a reduced life span when mated, while wet season males do not. Thus, reciprocal patterns of sexual selection through the seasons result in mutual ornamentation.

CREDITS (TOP TO BOTTOM): KRUTA & LETHIERS, UMR 7207; LIMA *ET AL.*

Published by AAAS

3C) quantitatively reproduce the main features discussed above. Inspection of the trajectories responsible for the side-lobes shows that these trajectories can indeed be considered as a reference and scattered wave packet, creating a hologram (Fig. 4A).

The efficiency of electron-ion recollision drops dramatically with increasing λ_{laser} because of spreading of the wave packet between ionization and recollision. Still, a clear hologram can be observed at 7 μm. Two effects make this possible. First, the hologram results from a heterodyne experiment, in which a weaker signal is mixed with a stronger signal. Second, to create a clear reference a large-impact parameter is needed in order to limit the interaction with the Coulomb field. For large λ_{laser}, a small p_r already leads to large-impact parameters because of the long excursion time between ionization and recollision.

Inspection of the electron trajectories contributing to the transverse structures (Fig. 3) reveals that they are due to recollision events in which the scattering does not occur on the first opportunity but on the second or third (*20*, *24*, *25*). Typical examples of these trajectories are shown in Fig. 4, B to D. One, respectively two glancing electron-ion collisions can be observed before the real recollision takes place. Usually, these rare events do not leave an imprint on the photoelectron spectrum. However, the combination of a long laser wavelength and Coulomb focusing (*24*) increases the probability because a small deviation introduced by the Coulomb potential can be sufficient to focus the returning wave packet onto the ion.

In our model study on the ionization of metastable xenon, we have experimentally shown the possibility to record holographic structures. Furthermore, our theoretical exploration shows that the hologram stores spatial and temporal information about the core- and electron dynamics. This offers opportunities to extend strong-field holography to more complicated systems and to use it to time-resolve electron-dynamics. As revealed in recent experiments (*6*, *26*), electron-ion recollision phenomena encode hole dynamics that occur in ions during the first few femtoseconds after strong-field ionization. When properly implemented with the use of a long-wavelength-driving laser, photo-electron holography appears especially well suited for studying this type of dynamics, in particular in molecules with a low binding energy that cannot easily be studied by other means.

References and Notes

1. P. B. Corkum, *Phys. Rev. Lett.* **71**, 1994 (1993).
2. F. Krausz, M. Y. Ivanov, *Rev. Mod. Phys.* **81**, 163 (2009).
3. M. F. Kling, M. J. J. Vrakking, *Annu. Rev. Phys. Chem.* **59**, 463 (2008).
4. J. Itatani *et al.*, *Nature* **432**, 867 (2004).
5. D. Shafir, Y. Mairesse, D. M. Villeneuve, P. B. Corkum, N. Dudovich, *Nat. Phys.* **5**, 412 (2009).
6. O. Smirnova *et al.*, *Nature* **460**, 972 (2009).
7. S. Baker *et al.*, *Science* **312**, 424 (2006).
8. M. Meckel *et al.*, *Science* **320**, 1478 (2008).
9. M. Spanner, O. Smirnova, P. B. Corkum, M. Y. Ivanov, *J. Phys. At. Mol. Opt. Phys.* **37**, L243 (2004).
10. H. Niikura *et al.*, *Nature* **417**, 917 (2002).
11. D. Gabor, *Nobel Lectures, Physics 1971-1980* (World Scientific, Singapore, 1992).
12. G. G. Paulus *et al.*, *Phys. Rev. Lett.* **84**, 3791 (2000).
13. J. Mauritsson *et al.*, *Phys. Rev. Lett.* **100**, 073003 (2008).
14. Materials and methods are available as supporting material on *Science* Online.
15. W. Becker, A. Lohr, M. Kleber, *J. Phys. At. Mol. Opt. Phys.* **27**, L325 (1994).
16. M. Lewenstein, K. C. Kulander, K. J. Schafer, P. H. Bucksbaum, *Phys. Rev. A* **51**, 1495 (1995).
17. J. M. Bakker *et al.*, *J. Chem. Phys.* **132**, 074305 (2010).
18. A. T. J. B. Eppink, D. H. Parker, *Rev. Sci. Instrum.* **68**, 3477 (1997).
19. B. R. Yang *et al.*, *Phys. Rev. Lett.* **71**, 3770 (1993).
20. G. G. Paulus, W. Becker, W. Nicklich, H. Walther, *J. Phys. At. Mol. Opt. Phys.* **27**, L703 (1994).
21. R. Gopal *et al.*, *Phys. Rev. Lett.* **103**, 053001 (2009).
22. H. G. Muller, *Laser Phys.* **9**, 138 (1999).
23. S. V. Popruzhenko, D. Bauer, *J. Mod. Opt.* **55**, 2573 (2008).
24. T. Brabec, M. Y. Ivanov, P. B. Corkum, *Phys. Rev. A* **54**, R2551 (1996).
25. G. L. Yudin, M. Y. Ivanov, *Phys. Rev. A* **63**, 033404 (2001).
26. Y. Mairesse *et al.*, *Phys. Rev. Lett.* **104**, 213601 (2010).

27. We acknowledge R. Kemper, H. Schoenmaker, A. de Snaijer, I. Cerjak, and the staff at the FELIX facility for their great technical assistance. This work is part of the research program of FOM, which is financially supported by the Nederlandse organisatie voor Wetenschappelijk Onderzoek (NWO). K.J.S. is supported by NSF grant PHY-0701372 and the Ball Professorship at LSU. M.Y.I. is supported by Science and Innovation grant EP/E036112/1 of the Engineering and Physical Sciences Research Council. O.S. acknowledges a Leibniz SAW award.

Supporting Online Material

www.sciencemag.org/cgi/content/full/science.1198450/DC1
Materials and Methods
SOM Text
Figs. S1 to S5
References

29 September 2010; accepted 7 December 2010
Published online 6 December 2010;
10.1126/science.1198450

Spin Crossover in Ferropericlase at High Pressure: A Seismologically Transparent Transition?

Daniele Antonangeli,[1,2]* Julien Siebert,[1,2] Chantel M. Aracne,[2] Daniel L. Farber,[2,3] A. Bosak,[4] M. Hoesch,[4] M. Krisch,[4] Frederick J. Ryerson,[2] Guillaume Fiquet,[1] James Badro[1,2]

Seismic discontinuities in Earth typically arise from structural, chemical, or temperature variations with increasing depth. The pressure-induced iron spin state transition in the lower mantle may influence seismic wave velocities by changing the elasticity of iron-bearing minerals, but no seismological evidence of an anomaly exists. Inelastic x-ray scattering measurements on ($Mg_{0.83}Fe_{0.17}$)O-ferropericlase at pressures across the spin transition show effects limited to the only shear moduli of the elastic tensor. This explains the absence of deviation in the aggregate seismic velocities and, thus, the lack of a one-dimensional seismic signature of the spin crossover. The spin state transition does, however, influence shear anisotropy of ferropericlase and should contribute to the seismic shear wave anisotropy of the lower mantle.

The characterization of pressure- and temperature-induced transformations in mantle minerals and their connection to seismic discontinuities aid in the understanding of Earth's interior. In this sense, the series of phase transformations that occurs in olivine—which with increasing pressure first transforms to wadsleyite, then to ringwoodite, and then breaks down into ferropericlase and perovskite—is emblematic. These phase changes are accompanied by density and sound-velocity variations that are responsible for the main seismic discontinuities in the upper mantle (*1*).

In contrast, the recently discovered iron spin-state transition—where compression favors the electron spin pairing, with the system changing from a high-spin to a low-spin state—in both ferropericlase (*2*) and perovskite (*3*), the two main phases of the lower mantle, does not clearly relate to any seismic signature, although effects on mantle density and seismic wave velocity have been anticipated (*4*–*8*). In ferropericlase, the spin transition occurs without structural changes (*4*, *9*), but experimental (*10*) and theoretical (*11*) studies suggest large softening of all the elastic moduli and, consequently, a major decrease in the aggregate sound velocities. Thus, at pressure and temperature conditions of the lower mantle, such an effect should be associated to a broad seismic anomaly (*12*) that, conversely, is not observed (*13*, *14*).

Here we present inelastic x-ray scattering (IXS) measurements on ($Mg_{0.83}Fe_{0.17}$)O-ferropericlase across the spin transition and up to 70 GPa (*15*). We obtained the complete elastic tensor (that is,

[1]Institut de Minéralogie et de Physique des Milieux Condensés, UMR CNRS 7590, Institut de Physique du Globe de Paris, Université Pierre et Marie Curie, Université Paris Diderot, 75005 Paris, France. [2]Lawrence Livermore National Laboratory, Livermore, CA 94550, USA. [3]Department of Earth and Planetary Sciences, University of California, Santa Cruz, Santa Cruz, CA, 95064, USA. [4]European Synchrotron Radiation Facility, BP 220, 38043 Grenoble Cedex, France.

*To whom correspondence should be addressed. E-mail: daniele.antonangeli@impmc.upmc.fr

all of the independent moduli that linearly relate stress and strain) and derived the aggregate sound velocities, the aggregate elastic moduli, and the shear anisotropy at corresponding depth. IXS has proven to be a useful technique for the high-pressure and high-temperature study of elasticity and sound velocities of powders (*16*–*18*) and single crystals (*19*, *20*). In particular, IXS allows all of the independent elements of the elastic tensor to be directly determined from the initial slope of the phonon dispersion of selected longitudinal acoustic (LA) and transverse acoustic (TA) modes, without any external input or a priori model (*15*). Thus, IXS overcomes the limitations of previously used surface-sensitive techniques [such as impulsive stimulated light scattering (ISLS) (*8*, *21*)] that require a complex data inversion, involving modeling of the sound waves at the interfaces and input of external parameters to obtain bulk properties. Brillouin measurements, which also directly provide sound velocities, were limited in the case of ferropericlase to the only shear velocities and the longitudinal moduli computed after input of the (independently measured) bulk modulus (*22*). IXS allows for the in situ determination of sample density (*15*), which is an important parameter in the mixed-spin region. Furthermore, whereas Brillouin scattering is restricted to transparent samples (*22*–*24*), IXS is not. Thus, we have been able to investigate high–iron-content ferropericlase [17 mole percent (mol %) Fe], which is more relevant to the lower mantle than that used in recent work (*8*, *22*–*24*).

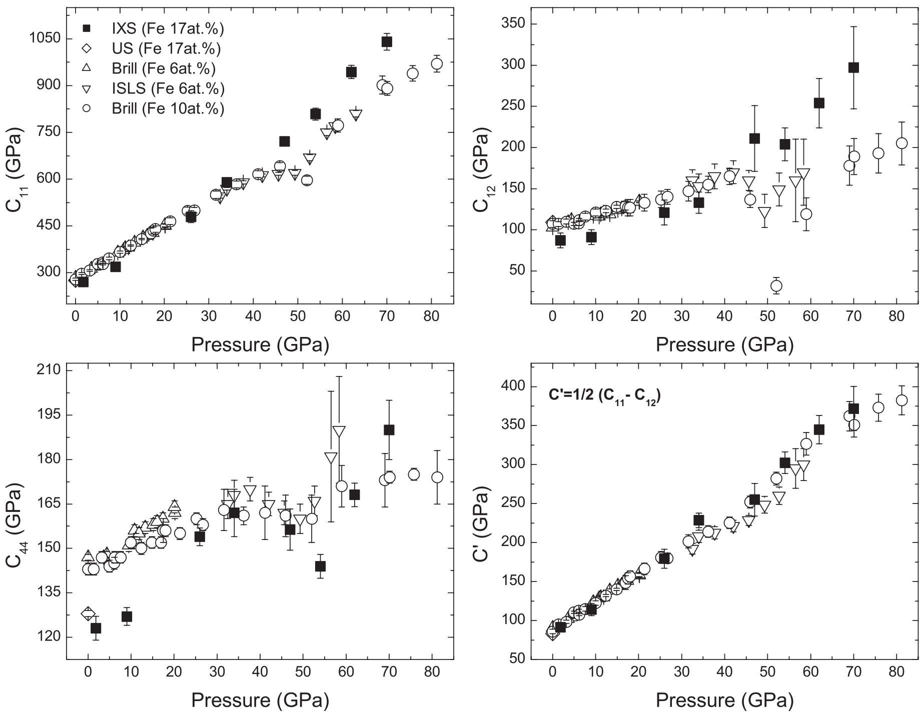

Fig. 1. Pressure evolution of the single-crystal elastic moduli of $(Mg_{1-x},Fe_x)O$-ferropericlase (table S1) (*15*). Solid squares, IXS data for $x = 0.17$ (this work); open diamonds, ambient pressure ultrasonic determinations for $x = 0.17$ (*26*); open triangles, Brillouin measurements for $x = 0.06$ (*23*); open inverted triangles, ISLS results for $x = 0.06$ (*10*); open circles, Brillouin determinations for $x = 0.10$ (*22*). Error bars account for the uncertainties on the measured velocities and densities (*15*). at. %, atomic percent.

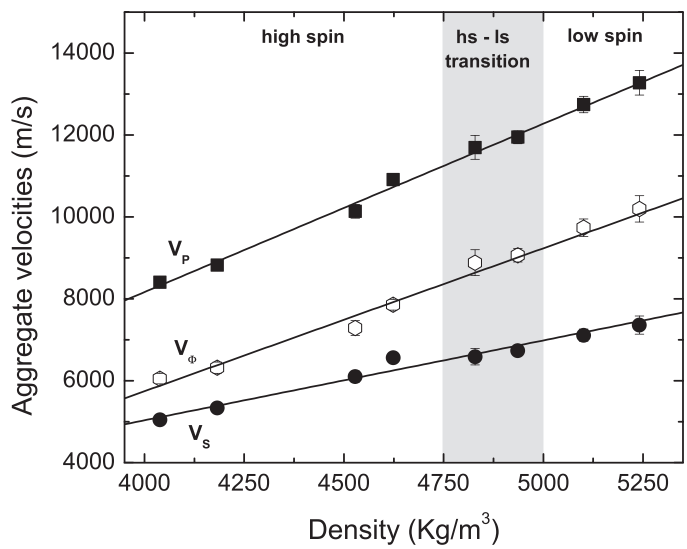

Fig. 2. Density evolution of the aggregate sound velocities (Voigt-Reuss-Hill average) (*15*). Solid squares, compressional sound velocity (V_P); solid circles, shear sound velocity (V_S); open hexagons, bulk sound velocity ($V_\Phi = \sqrt{K/\rho}$). The lines are linear fits to the experimental data. The density range corresponding to the spin-transition zone (4750 to 5000 kg/m^3) is shaded. Error bars on the aggregate velocities come from the propagation of the uncertainties on the elastic moduli and the difference between the Voigt and Reuss average (*15*).

Up to ~40 GPa, all the elastic moduli exhibit a monotonic increase with pressure (Fig. 1 and table S1), as is expected with compression. In the 40–to–60-GPa pressure range, where the spin transition occurs (*2*, *4*, *25*), we observe a distinct softening of C_{44} and a small variation in C_{12}, whereas C_{11} retains a continuous trend. Above 60 GPa, the usual monotonic increase with pressure is observed for all of the moduli, albeit with a larger pressure derivative. The back extrapolations of our results to ambient pressure are within a few percent of the ultrasonic determinations for the same composition (*26*). However, if we compare our high-pressure measurements with ISLS (*10*) and Brillouin (*22*, *24*) data obtained on samples with lower iron content, we observe qualitative agreement for C_{44} and $C' = 1/2(C_{11} - C_{12})$, which display softening in the pressure range of the spin transition for all methods (quantitative differences are at least partially due to differences in iron concentration), but disagreement for C_{12} and C_{11}. Whereas both optical studies (*8*, *22*) report a large softening of C_{11} in the 40–to–60-GPa range, the direct determination of C_{11} by IXS [via sound velocity measurements of the LA[100] mode (*15*)] does not show any anomaly (Fig. 1). To support our findings, we stress that in other systems where pressure-induced, spin-pairing transitions occur (such as the extensively investigated Fe-, Co-, and Mn-Invar alloys), these transitions are commonly accompanied by much larger effects on the shear elastic moduli than on the longitudinal moduli (*27*, *28*).

From the measured single-crystalline C_{ij}, we computed the aggregate elastic properties bulk and shear moduli, as well as the compressional (V_P) and shear (V_S) sound velocities by straightforward averaging [see (*15*)]. The values we obtain for the bulk and shear moduli compare favorably with the ambient-pressure ultrasonic determination (*26*) and with the values obtained by x-ray diffraction (*4*) for both the low-spin and the high-spin state (figs. S3 and S4).

A direct consequence of the lack of softening of C_{11} and of the moderate effect on C_{12} is the absence of any sizable deviation from a linear density evolution of the aggregate V_P and V_S (Fig. 2). In contrast to recent claims (*8*, *11*, *22*), neither V_P nor V_S show an anomaly due to the spin-pairing transition.

With respect to Earth's lower mantle, recent optical (*8*, *22*) and theoretical (*11*) studies proposed that an anomalous (albeit smooth) softening of the aggregate elastic properties (especially the bulk modulus K and the bulk velocity $V_\Phi = \sqrt{K/\rho}$, where ρ is density) should occur at depth. The range over which this takes place has been suggested to extend from 1000 to 1500 km, based on room-temperature results (*8*), and from 1300 to 1800 km, when including high-temperature effects (*22*), such as those along a mantle geotherm (*11*). Our study provides an explanation for the lack of a seismic signature (*13*, *14*) associated with the spin crossover in the lower mantle.

The high-spin–to–low-spin transition does, however, have an effect on the single-crystal elasticity of ferropericlase (when not smeared due to averaging over many grains as in an ideally random aggregate). The relative magnitude of the shear elastic moduli C_{44} and C' (corresponding to the sound velocity of the $TA[110]_{<001>}$ and $TA[110]_{<-110>}$ modes, respectively) evolves with pressure (Fig. 3). At ambient and low pressures, $C_{44} > C'$, but the pressure derivative of C' is larger than that of C_{44}, so that the two intersect around 16 to 17 GPa. At higher pressures, the sign of shear anisotropy is reversed. This behavior is in good agreement with results of Brillouin spectroscopy on samples with 10 mol % Fe (*24*). Above 60 GPa, in the low-spin phase, the pressure derivative of the two shear moduli is almost the same. Accordingly, the pressure evolution of the shear anisotropy, defined as $A = 2(C' - C_{44})/(C' + C_{44})$, is very different for the high- and low-spin ferropericlase (see inset of Fig. 3): A increases linearly with pressure in the high-spin phase, whereas it remains almost constant (or slightly decreases) in the low-spin phase. Thus, we suggest that a seismically detectable signature of the spin transition in the lower mantle may be found in the shear anisotropy. Because ferropericlase is much weaker than perovskite, it can accommodate most of the strain (*29*) and develop strong texture (*30*). Our measurements indicate a very large shear anisotropy, ~70% at 70 GPa for ferropericlase with a Fe content of 17 mol %, a value very close to that measured for ferropericlase with 10 mol % Fe (*24*) and at least 50% larger than the shear anisotropy of MgO (*24*). Such a considerable anisotropy, in conjunction with lattice-preferred orientation, supports the notion that ferropericlase is the main phase responsible for the seismic shear anisotropy of the lower mantle (*24*). Therefore, the different shear anisotropy behavior of high- and low-spin ferropericlase should be considered together with temperature and chemical variations to interpret local seismic heterogeneity.

Finally, the values of V_P and V_S for $(Mg_{0.83}Fe_{0.17})O$-ferropericlase at 70 GPa (13300 ± 300 m/s and 7360 ± 220 m/s, respectively) are very close to the measured V_S (*31*) and computed V_P and V_S (*32*, *33*) values for $MgSiO_3$-perovskite at the same pressure. Because both Fe and Al are expected to lower the aggregate velocities of perovskite (*33*, *34*), our results suggest that the velocities of the two major phases of the lower mantle might become comparable (if not ferropericlase faster than perovskite) in the lowermost 1000 to 1200 km of the lower mantle. This could challenge current compositional models of the lowermost mantle based on an extrapolation of lower-pressure elasticity data. However, direct high-pressure, high-temperature measurements on both ferropericlase and perovskite (with relevant major-element compositions) are required to confirm these conjectures.

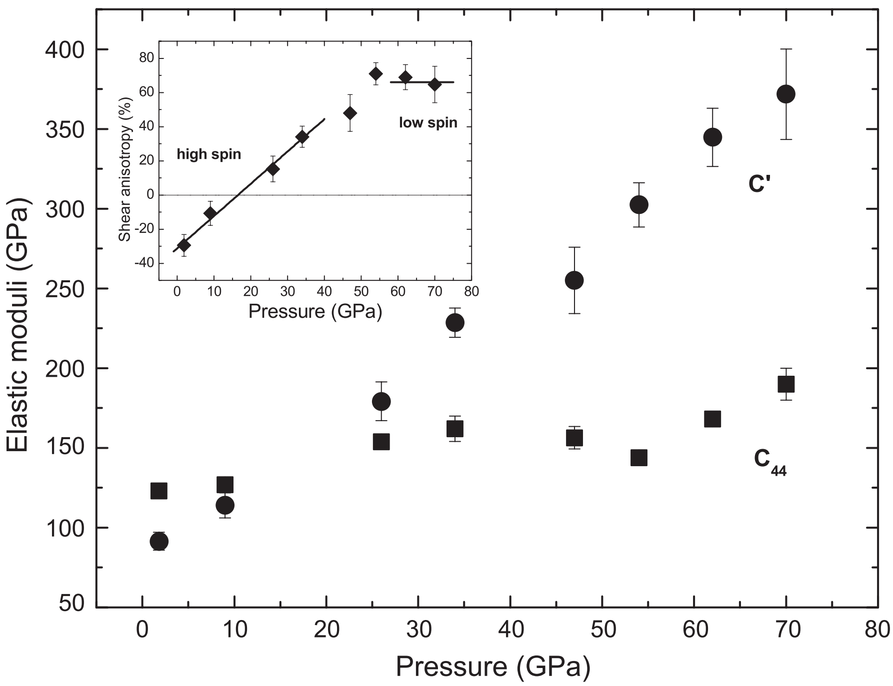

Fig. 3. Comparison of the pressure evolution of C_{44} (squares) and C' (circles), corresponding to the two different polarizations of the shear mode in the diagonal plane of a cubic lattice. (**Inset**) Shear anisotropy as a function of pressure. The lines are guides for the eye. Error bars account for the uncertainties on the measured velocities and densities (*15*).

References and Notes

1. J.-P. Poirier, *Introduction to the Physics of the Earth's Interior* (Cambridge Univ. Press, Cambridge, 2000).
2. J. Badro *et al.*, *Science* **300**, 789 (2003); 10.1126/science.1081311.
3. J. Badro *et al.*, *Science* **305**, 383 (2004).
4. J.-F. Lin *et al.*, *Nature* **436**, 377 (2005).
5. J.-F. Lin *et al.*, *Geophys. Res. Lett.* **33**, L22304 (2006).
6. J.-F. Lin *et al.*, *Geophys. Res. Lett.* **34**, L09301 (2007).
7. S. Speziale *et al.*, *J. Geophys. Res.* **112**, B10212 (2007).
8. K. Catalli *et al.*, *Earth Planet. Sci. Lett.* **289**, 68 (2010).
9. Y. Fei *et al.*, *Geophys. Res. Lett.* **34**, L17307 (2007).
10. J. C. Crowhurst, J. M. Brown, A. F. Goncharov, S. D. Jacobsen, *Science* **319**, 451 (2008).
11. R. M. Wentzcovitch *et al.*, *Proc. Natl. Acad. Sci. U.S.A.* **106**, 8447 (2009).
12. J.-F. Lin *et al.*, *Science* **317**, 1740 (2007).
13. G. Masters, *Eos Trans. AGU* **89** (53), Fall Meet. Suppl., abstr. MR23A-04 (2008).
14. F. Cammarano, H. Marquardt, S. Speziale, P. J. Tackley, *Geophys. Res. Lett.* **37**, L03308 (2010).
15. Materials and methods are available as supporting material on *Science* Online.
16. D. Antonangeli *et al.*, *Earth Planet. Sci. Lett.* **225**, 243 (2004).
17. D. Antonangeli *et al.*, *Phys. Rev. B* **72**, 134303 (2005).
18. D. Antonangeli *et al.*, *Earth Planet. Sci. Lett.* **295**, 292 (2010).
19. D. Antonangeli *et al.*, *Phys. Rev. Lett.* **93**, 215505 (2004).
20. D. Antonangeli, M. Krisch, D. L. Farber, D. G. Ruddle, G. Fiquet, *Phys. Rev. Lett.* **100**, 085501 (2008).
21. J. C. Crowhurst *et al.*, *Appl. Phys. Lett.* **89**, 111920 (2006).
22. H. Marquardt, S. Speziale, H. J. Reichmann, D. J. Frost, F. R. Schilling, *Earth Planet. Sci. Lett.* **287**, 345 (2009).
23. J. M. Jackson *et al.*, *J. Geophys. Res.* **111**, B09203 (2006).
24. H. Marquardt *et al.*, *Science* **324**, 224 (2009).
25. A. F. Goncharov, V. V. Struzhkin, S. D. Jacobsen, *Science* **312**, 1205 (2006).
26. S. D. Jacobsen *et al.*, *J. Geophys. Res.* **107**, 2037 (2002).
27. F. Decremps, L. Nataf, *Phys. Rev. Lett.* **92**, 157204 (2004).
28. L. Nataf, F. Decremps, M. Gauthier, G. Syfosse, *Ultrasonics* **44** (suppl. 1), e555 (2006).
29. K. Madi, S. Forest, P. Cordier, M. Boussuge, *Earth Planet. Sci. Lett.* **237**, 223 (2005).
30. C. E. Tommaseo, J. Devine, S. Merkel, S. Speziale, H. K. Wenk, *Phys. Chem. Miner.* **33**, 84 (2006).
31. M. Murakami, S. Sinogeikin, H. Hellwig, J. Bass, J. Li, *Earth Planet. Sci. Lett.* **256**, 47 (2007).
32. A. R. Oganov, J. P. Brodholt, G. D. Price, *Earth Planet. Sci. Lett.* **184**, 555 (2001).
33. B. Kiefer, L. Stixrude, R. M. Wentzcovitch, *Geophys. Res. Lett.* **29**, 1539 (2002).

34. J. M. Jackson, J. Zhang, J. Shu, S. V. Sinogeikin, J. D. Bass, *Geophys. Res. Lett.* **32**, L21305 (2005).
35. We thank F. Occelli, G. Le Marchand, P. Munsch, P. Bouvier, M. Hanfland, M. Mezouar, and A. L. Auzende for experimental help. This work was performed under the auspices of the U.S. Department of Energy and Lawrence Livermore National Laboratory under contract DE-AC52-07NA27344 and was supported by the Office of Basic Energy Sciences–Geosciences Research Program (F.J.R.). D.A., J.B., and J.S. acknowledge financial support from the European Research Council (ERC) under the European Community's Seventh Framework Programme (FP7/2007-2013)/ERC grant agreement no. 207467. This work was supported by the French National Research Agency grant no. ANR-07-BLAN-0124-01 and ERC grant agreement no. 207467.

Supporting Online Material
www.sciencemag.org/cgi/content/full/331/6013/64/DC1
Materials and Methods
Figs. S1 to S4
Table S1
References and Notes

28 September 2010; accepted 6 December 2010
10.1126/science.1198429

Small Interannual Variability of Global Atmospheric Hydroxyl

S. A. Montzka,[1]* M. Krol,[2,3] E. Dlugokencky,[1] B. Hall,[1] P. Jöckel,[4]† J. Lelieveld[4,5]

The oxidizing capacity of the global atmosphere is largely determined by hydroxyl (OH) radicals and is diagnosed by analyzing methyl chloroform (CH_3CCl_3) measurements. Previously, large year-to-year changes in global mean OH concentrations have been inferred from such measurements, suggesting that the atmospheric oxidizing capacity is sensitive to perturbations by widespread air pollution and natural influences. We show how the interannual variability in OH has been more precisely estimated from CH_3CCl_3 measurements since 1998, when atmospheric gradients of CH_3CCl_3 had diminished as a result of the Montreal Protocol. We infer a small interannual OH variability as a result, indicating that global OH is generally well buffered against perturbations. This small variability is consistent with measurements of methane and other trace gases oxidized primarily by OH, as well as global photochemical model calculations.

The hydroxyl radical (OH) is the primary oxidant for many non-CO_2 greenhouse gases, several stratospheric ozone-depleting substances and their substitutes, and hazardous air pollutants. It is also central to atmospheric photochemistry and the regulation of tropospheric ozone, and thus controls the influence of chemically reduced trace gases on climate, the stratospheric ozone layer, and air quality (*1–4*). The interannual variability (IAV) in OH concentrations ([OH]) on large spatial scales provides insight into the stability of the atmospheric oxidation capacity and its sensitivity to human-induced and natural perturbations. However, a consistent, predictive understanding of the net response of [OH] on broad scales to such perturbations is lacking. For example, a range of negative [OH] feedbacks is calculated from changes in atmospheric methane abundance (*3*, *5–7*).

Theory suggests that the sensitivity of [OH] to environmental changes depends on the relative importance of primary and secondary (recycling) OH formation pathways (*7*). The balance between primary OH formation initiated by ultraviolet light and formation by recycling is determined by atmospheric abundances and distributions of NO_x, H_2O, O_3, CO, and CH_4, as well as other parameters (*3*, *8*), many of which are highly variable in space and time and are relatively poorly characterized on global scales and in model calculations. As a result, calculated sensitivities of global [OH] to IAV in the chemical and physical makeup of the atmosphere have yet to be adequately tested.

Although OH can be measured directly on local scales, these results cannot characterize the integrated response of global mean [OH] to the many processes that control its formation and loss. Instead, indirect techniques are used in which [OH] is derived from observations of OH-oxidized trace gases such as CH_3CCl_3 and ^{14}CO (*9–19*). However, these approaches can suggest a very different sensitivity of [OH] to variations in the atmospheric environment than is derived in atmospheric models (*20*). Year-to-year changes in global [OH] as high as 20 to 25% have been derived from analyses of CH_3CCl_3 observations between 1980 and 2003, and these analyses imply a mean IAV of 7 to 9% (*16*, *17*). Chemistry transport models calculate a global [OH] variability of only 1 to 2%, but these models do not currently include variability in all factors influencing [OH] (*20–23*). Variations in [OH] of up to 20% have been estimated from ^{14}CO, although only over a few months and on semihemispheric spatial scales (*19*).

Global mean [OH] can be estimated from atmospheric observations of a trace gas whose predominant sink is reaction with OH from mass balance considerations by equating the rate of change in the global burden (*dG/dt*) to the difference between the global emission rate (*E*) and loss. Solving for the pseudo–first-order rate constant for loss (k_G), which is proportional to [OH], gives

$$[\mathrm{OH}] \propto k_G = \frac{E}{G} - \frac{dG/dt}{G} \tag{1}$$

where *G* is the global burden estimated from surface measurements. Although CH_3CCl_3 losses (and k_G) are dominated by OH oxidation according to $k(T) \times [\mathrm{OH}]$, they include stratospheric photolysis, hydrolysis in surface waters, and other processes. Global mean [OH] derived in this

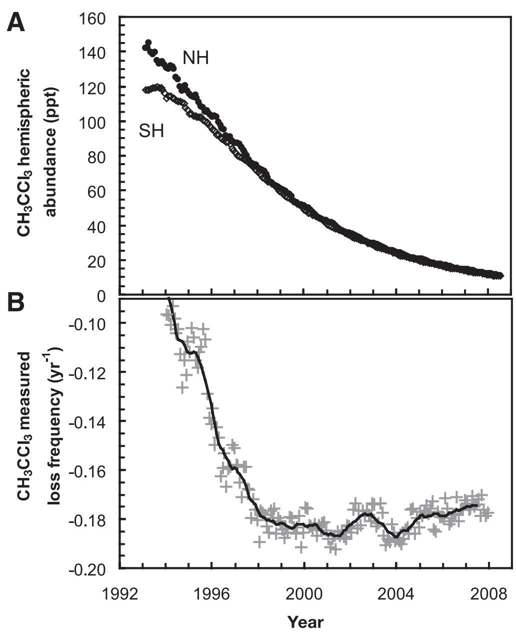

Fig. 1. (**A**) Observed hemispheric monthly mean mixing ratios of CH_3CCl_3 [update of (*14*)]. NH and SH denote Northern and Southern Hemispheres, respectively. (**B**) Exponential loss frequencies for CH_3CCl_3 derived from global surface means. Gray points are independent estimates derived from monthly means 12 months apart [e.g., $\ln(G_{\mathrm{Jan.}\ 2007}/G_{\mathrm{Jan.}\ 2006})$] plotted at the midpoint of this interval; the black line is the 12-month running mean.

[1]NOAA Earth System Research Laboratory, Boulder, CO 80305, USA. [2]Institute for Marine and Atmospheric Research Utrecht, University of Utrecht, 3584 CC Utrecht, Netherlands. [3]Meteorology and Air Quality Group, Wageningen University, 6708 PB Wageningen, Netherlands. [4]Department of Atmospheric Chemistry, Max Planck Institute for Chemistry, D-55128 Mainz, Germany. [5]Cyprus Institute, Nicosia 1645, Cyprus.

*To whom correspondence should be addressed. E-mail: stephen.a.montzka@noaa.gov
†Present address: Deutsches Zentrum für Luft- und Raumfahrt, Institut für Physik der Atmosphäre, Oberpfaffenhofen, D-82234 Wessling, Germany.

www.sciencemag.org/cgi/content/full/331/6013/64/DC1

Supporting Online Material for

Spin Crossover in Ferropericlase at High Pressure: A Seismologically Transparent Transition?

Daniele Antonangeli,* Julien Siebert, Chantel M. Aracne, Daniel L. Farber, A. Bosak, M. Hoesch, M. Krisch, Frederick J. Ryerson, Guillaume Fiquet, James Badro

*To whom correspondence should be addressed. E-mail: daniele.antonangeli@impmc.upmc.fr

Published 7 January 2011, *Science* **331**, 64 (2011)
DOI: 10.1126/science.1198429

This PDF file includes:

Materials and Methods
Figs. S1 to S4
Table S1
References and Notes

Supporting Online Material for

Spin crossover in ferropericlase at high pressure: a seismologically transparent transition?

D. Antonangeli*, J. Siebert, C.M. Aracne, D.L. Farber, A. Bosak, M. Hoesch, M. Krisch, F.J. Ryerson, G.Fiquet, J. Badro

* To whom correspondence should be addressed. Email: daniele.antonangeli@impmc.upmc.fr

This PDF file includes:

Materials and Methods
Figures S1 to S4
Table S1

Materials and Methods

Sample synthesis and characterization

Oriented single crystals of $(Mg_{1-x}Fe_x)O$-ferropericlase, were synthesized at the Lawrence Livermore National Laboratory starting from a pre-aligned crystal of MgO (normal parallel to [110] direction) by high-temperature Fe-Mg interdiffusion in a piston cylinder press (1400° C at 1 GPa for 200 hours). The oxygen fugacity was buffered close to the IW (Iron-Wüstite) buffer by loading the sample in an iron capsule. The resulting crystals were of excellent optical quality, with greenish colour, lighter or darker depending upon Fe content. Using a focused ion beam instrument (FIB), a 40 nm thick section was cut out of the recovered sample for electron energy loss spectroscopy measurement, and no detectable amount of ferric iron was measured. Samples with total iron content ≤ 25 at% prepared at ambient pressure close to the IW buffer can have $Fe^{3+}/\Sigma Fe$ up to 2% (S1). Since high pressure is known to destabilize Fe^{3+}, this estimation can be reasonably considered an upper limit four our samples, synthesized at 1 GPa.

The samples were polished to 15-20 μm thickness (as determined by optical interferometry in reflection spectra) and cut by fs laser to approximately 40 μm in diameter. Details of sample micro-maching are reported in S2. We produced $(Mg_{1-x}Fe_x)O$-ferropericlase samples with different iron contents, varying in the range x=0.13 to 0.21; the exact composition and chemical homogeneity was determined individually for each disk by electron microprobe analysis (operating conditions at 15 kV and 10 nA).

Samples with x=0.17 ($Fe^{3+}/\Sigma Fe$ <2%) were loaded for the IXS measurements in membrane driven diamond anvil cells, equipped with rhenium gaskets and either 300 or 250 μm culet diamonds, using neon as pressure transmitting medium to ensure quasi-hydrostatic compression. Data were collected data at 1.8, 9, 26, 34, 47, 54, 62 and 70 GPa, as determined by ruby fluorescence (see Table S1). Typical mosaic spread (rocking curves) yielded 0.2° FWHM. No degradation was observed with increasing pressure up to ~35 GPa. At higher pressures the rocking curves got larger, with a maximum broadening to ~2° FWHM at 70 GPa.

Inelastic x-ray scattering measurements

The IXS experiment was performed on beamline ID28 at the European Synchrotron Radiation Facility, in Grenoble. We utilized the silicon (9 9 9) configuration at 17794 eV, yielding an overall energy resolution of 3 meV full-width-half-maximum (FWHM), and the focusing optics in Kirkpatrick-Baez configuration with a focal spot size at the sample of 30x90 μm^2 (horizontal x vertical, FWHM). Beamsize was further reduced by slits in the vertical direction to 40 μm to match sample dimensions. Direction and size of the momentum transfer, q, were selected by an appropriate choice of the scattering angle and the sample orientation in the horizontal scattering plane. The momentum resolution was typically set to 0.28 and 0.84 nm^{-1} in the horizontal and vertical plane. Further details of the beamline configuration can be found elsewhere (S3). Examples of the collected spectra are illustrated in Figure S1.

To redundantly constrain all the elements of the elastic tensor (namely C_{11}, C_{12} and C_{44}) we measured the low-q portion (linear part) of the phonon dispersion of four to five modes: longitudinal acoustic (LA) along [100] and [110], transverse acoustic (TA) along [100], and [110], both polarized <001> and polarized <-110>. Typically, two to three IXS spectra were recorded in the low q part of the acoustic phonon branch, and the sound velocity V was determined by a linear fit to the E(q) values with an error of 1–2% (see Figure S2), and related to the elastic moduli via the Christoffel equation (S4). Specifically:

$V_{LA}[100] = (C_{11} / \rho)^{1/2}$

$V_{TA}[100] = (C_{44} / \rho)^{1/2}$

$V_{LA}[110] = (C_{11}+C_{12}+2C_{44} / 2\rho)^{1/2}$

$V_{TA}[110]_{<001>} = (C_{44} / \rho)^{1/2}$

$V_{TA}[100]_{<-110>} = (C' / \rho)^{1/2} = (C_{11}-C_{12} / 2\rho)^{1/2}$

Bragg angles of the [111], [002], and [220] reflections were also recorded, in order to provide the crystal orientation matrix and a direct determination of the density for each pressure point. This independent measurement yielded values in agreement with published equation of state (S5).

We collected data at 1.8, 9, 26, 34, 47, 54, 62 and 70 GPa, as determined by ruby fluorescence. Our results are summarized in Table S1.

Single crystalline elastic moduli and aggregate elastic properties

We derived the aggregate elastic properties (bulk and shear modulus, compressional and shear sound velocities) starting from the values of the single crystalline elastic moduli C_{ij} both under Voigt (iso-strain) and Reuss (iso-stress) approximations (S6,S7). The two estimates, which provide an upper (Voigt) and lower (Reuss) bound for the aggregate, differ appreciably (more than 2%) only above 45 GPa. In our discussion we considered the arithmetical mean of the two (Hill approximation (S8)). The obtained values for the bulk and shear modulus are reported as a function of pressure in Figure S3 and Figure S4, together with the ultrasonic ambient pressure determination (S9) and the values obtained by x-ray diffraction (S5) on samples of same composition. We can observe a kink in the pressure evolution of the shear modulus (Figure S4) as a direct consequence of the large softening of C_{44}, while the bulk modulus exhibits a smooth continuous behavior (Figure S3).

Supporting online figures

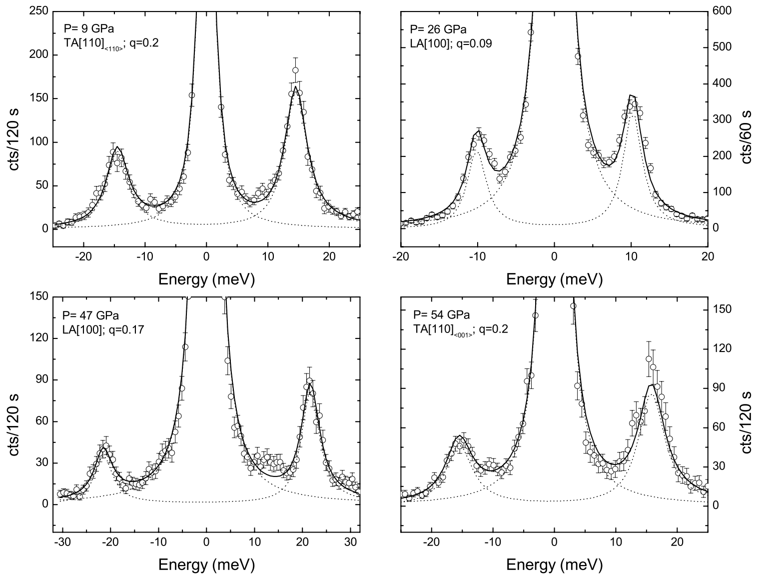

Figure S1: Representative IXS spectra. The experimental data are shown together with the best fit results (thick solid line) and the corresponding individual components (thin dotted lines). IXS spectra are characterized by an elastic contribution centered at zero energy and two symmetric features, the Stokes and anti-Stokes peaks of the ferropericlase acoustic phonons.

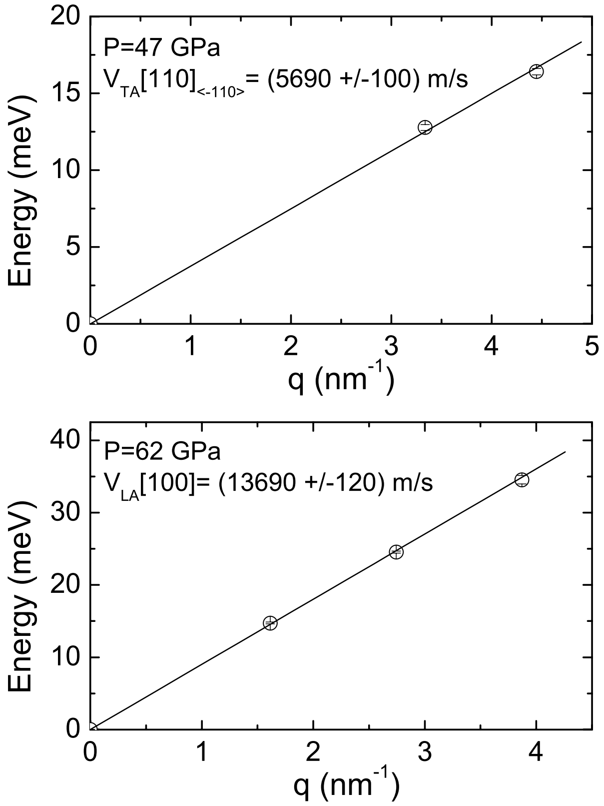

Figure S2: Examples of the linear fit to the initial slope of the phonon dispersion. Top: $TA[110]_{<-110>}$ at 47 GPa. Bottom: LA[100] at 62 GPa. The errors on velocities come from the statistical uncertainties of the liner fit.

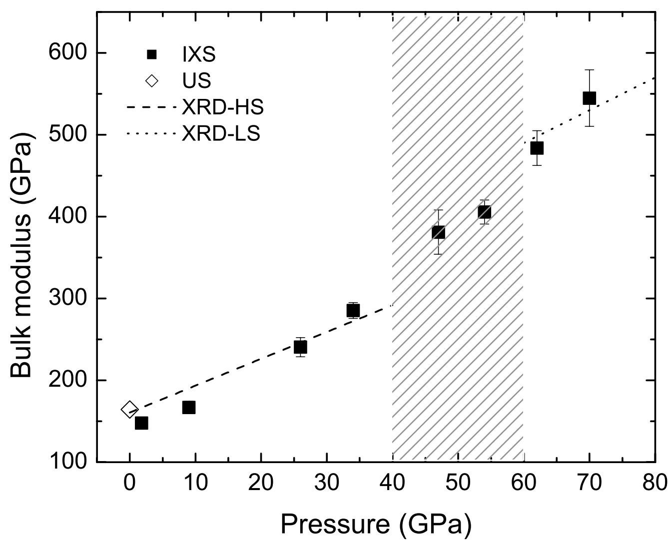

Figure S3: Bulk modulus as a function of pressure. IXS results (solid squares) are compared to ambient pressure ultrasonic determination (S9) (open diamond) and values derived from x-ray diffraction measurements (S5) (dashed line: high-spin state; dotted line: low-spin state). The pressure range corresponding to the spin transition zone is shaded in gray.

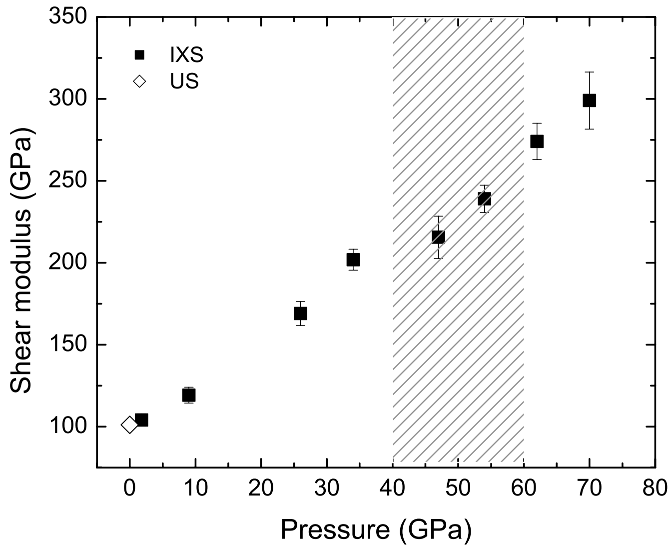

Figure S4: Shear modulus as a function of pressure. Solid squares: IXS results; open diamond: ambient pressure ultrasonic determination (S9). The pressure range corresponding to the spin transition zone is shaded in gray.

Supporting online table

Run	P	ρ	measured modes	C_{11}	C_{12}	C_{44}	C'
a	1.8	4039	LA[100]; LA[110]; TA[110]$_{<001>}$; TA[100]$_{<-110>}$	270±7	87±9	123±4	91±6
a	26	4528	LA[100]; LA[110]; TA[110]$_{<001>}$; TA[100]$_{<-110>}$	479±19	121±15	154±3	179±12
a	47	4829	LA[100]; LA[110]; TA[110]$_{<001>}$; TA[110]$_{<001>}$	721±12	211±40	156±7	255±21
a	54	4936	LA[100]; LA[110]; TA[110]$_{<001>}$; TA[100]$_{<-110>}$	809±19	204±20	144±4	302±14
a	62	5101	LA[100]; LA[110]; TA[100]; TA[110]$_{<001>}$	943±21	254±30	168±4	345±18
a	70	5241	LA[100]; TA[100]; LA[110]; TA[110]$_{<001>}$	1040±27	297±50	190±10	372±28
b	9	4183	LA[100]; TA[100]; LA[110]; TA[110]$_{<001>}$; TA[100]$_{<-110>}$	319±13	91±9	127±3	114±8
c	34	4623	LA[100]; TA[100]; LA[110]; TA[110]$_{<001>}$; TA[100]$_{<-110>}$	590±13	133±13	162±8	229±9

Table S1: Synopsis of the obtained results. All the values are in GPa, but for the densities, which are in Kg/m^3.

References and Notes for supporting online materials

S1. I. Srečec *et al.*, *Phys. Chem. Minerals* **14**, 492 (1987).

S2. D.L. Farber, D. Antonangeli, C.M. Aracne, J. Benterou, *High Press. Res.* **26**, 1 (2006).

S3. M. Krisch, *J. Raman Spectrosc.* **34**, 628 (2003).

S4. B. A. Auld, *Acoustic Fields and Waves in Solids* (J.Wiley and Sons, New York, 1973), Vol. 1.

S5. J.F. Lin *et al.*, *Nature* **436**, 377 (2005).

S6. W. Voigt, *Lehrbuch der Kristallphysik* (Teubner, Leipzig, 1928).

S7. A. Reuss, Z. Angew, *Math. Mech.* **9**, 55 (1929).

S8. R. Hill, *Proc. Phys. Soc., London, Sect. A* **65**, 349 (1952).

S9. S.D. Jacobsen *et al.*, *J. Geophys. Res.* **107**, 2307 (2002).

S10. The focused ion beam (FIB) facility of the Institut de Minéralogie et de Physique des Milieux Condensés is supported by Région Ile de France grant SESAME 2006 N°I-07-593/R, INSU-CNRS, INP-CNRS, University Pierre et Marie Curie – Paris 6, and by the French National Research Agency (ANR) grant no. ANR-07-BLAN-0124-01.